Automatic Recognition of General LPI Radar Waveform Using SSD and Supplementary Classifier

Linh Manh Hoang ⬤, Minjun Kim ⬤, and Seung-Hyun Kong ⬤, *Senior Member, IEEE*

Abstract—**For low probability of intercept (LPI) radars, frequency-modulated and phase-modulated continuous waveforms are widely used because of their low peak power compared to that of pulse waves (PW). However, there has been a limited number of studies on recognizing continuous wave (CW) LPI radar, in spite of its importance and popularity. In this paper, in order to recognize both PW and CW LPI radar waveforms, we propose an LPI radar waveform recognition technique (LWRT) based on a single-shot multi-box detector (SSD) and a supplementary classifier. It is demonstrated with Monte Carlo simulations that the proposed LWRT achieves classification performance similar to that of the current LWRT with the highest classification performance for PW LPI radar waveforms, even without the prior condition used in existing LWRTs. For CW LPI radar waveforms, on the other hand, with the combination of the SSD and the supplementary classifier, the proposed LWRT achieves extraordinary recognition performance for all 12 LPI radar modulation schemes (i.e., BPSK, Costas, LFM, Frank, P1, P2, P3, P4, T1, T2, T3, and T4) considered in the literature.**

Index Terms—**Waveform recognition, low probability of intercept, single shot multi-box detector.**

I. INTRODUCTION

LOW probability of intercept (LPI) radars that use particular modulated waveforms to prevent non-cooperative receivers from intercepting and detecting their emissions have become more and more popular in electronic warfare (EW) systems [1]. There are two types of waveforms used for LPI radar, continuous wave (CW) and pulse wave (PW), and the modulation schemes used by the LPI radars are classified into frequency modulation (FM) and phase modulation (PM) [2]. Since CW LPI radar spreads the signal energy over a much longer time interval than does PW LPI radar, its peak power is much smaller than that of PW LPI radar. The low peak power of CW LPI radar allows it

to stay silent against non-cooperative receivers, explaining the prevalence of use and significant advantages of this radar over PW LPI radar. Thus, a powerful LPI radar waveform recognition technique (LWRT) should have the ability to perceive not only PW but also CW.

[3] first introduces an LWRT based on multilayer perceptron (MLP) and features extracted from PW LPI radar signals. [4] adds more features and makes use of a recurrent neural network (RNN) to achieve higher LWRT performance. However, these studies [3], [4] have two main disadvantages. First, since the features calculated from the complex envelope (CE) of the signals are affected by the residual frequency caused by the carrier frequency estimation error (CFEE), there is dramatic performance degradation. Second, the LWRTs are signal dependent, such that the designed features depend on a modulation scheme to improve classification performance. As a result, when system attempts to recognize a new modulation scheme, the suitable features of the new modulation scheme must be developed.

Recently, in [5], [6], the authors use the Choi-William distribution (CWD) to generate time-frequency images (CWD-TFIs) as the input to the convolutional neural network (CNN) to recognize PW LPI radar waveforms. In particular, among the existing LWRTs, [5] achieves the highest classification performance for the twelve modulation schemes of PW LPI radar signals defined in [1]. One of the benefits of utilizing CNN is that the influence of CFEE becomes negligible; in fact, CFEE merely shifts the position of the signal objects in CWD-TFI; this shift does not degrade the performance of CNN. In addition, CNN recognizes LPI radar signals by determining the effective features of the signal objects in CWD-TFI automatically. Thus, when additional modulation schemes need to be considered, there is no need to manually design additional signal features specific to the modulation schemes. However, the computation cost of CWD increases dramatically as the signal size increases. To overcome this problem, [5] proposed a sample averaging technique (SAT) to increase the processing gain while maintaining the computation cost, whereas [7] utilized the fractional Fourier transform (FRT) to reduce the computational cost required for the employed TFA techniques such as Radon ambiguity transform (RAT) and Radon-WVD (RWT) [5].

In fact, the LWRTs in [3]–[5] are based on the assumption that the LPI radar pulse interval (i.e., between the beginning and ending sample points) can be precisely detected and the starting and ending points of the pulse interval are exactly known. This assumption is not realistic, because the intercepted signal can have low SNR, such that the detection of the pulse interval

L. M. Hoang is with the University of Technology Sydney, Ultimo, NSW 2007, Australia (e-mail: linh.m.hoang@student.uts.edu.au).

M. Kim is with the Korea Aerospace Research Institute, Daejeon 34133, South Korea (e-mail: minjunk@kari.re.kr).

S.-H. Kong is with the CCS Graduate School of Green Transportation, Korea Advanced Institute of Science and Technology, Daejeon 34141, South Korea (e-mail: skong@kaist.ac.kr).

may not be accurate or possible. In addition, the LWRTs in [3]–[5] are developed to recognize only PW LPI radar waveforms, not CW LPI radar waveforms, for the following two reasons. First, the LWRTs in [3], [4] use certain features, such as number of signal clusters in CWD-TFI for a single pulse interval and CWD time peak location, that are only useful to distinguish PW LPI radar waveforms, not CW LPI radar waveforms [3], [4]. In fact, the effective features to recognize CW LPI radar waveforms have seldom been studied. Second, the LWRT in [5] uses a CNN classifier that considers the whole image as the input and only classifies the whole content in the image. However, the CWD-TFIs of CW LPI radar signals may contain a number of consecutive periods of signal objects, and the signal objects in CWD-TFI may be difficult for the CNN to classify when the number of periods varies. For example, a CNN classifier trained by CWD-TFIs with two consecutive periods of signal objects often fails to classify when the CWD-TFI contains three consecutive periods of signal objects. Therefore, the CNN classifier is not suitable for CW LPI radar signals with varying numbers of periods. In this case, for higher performance, it is necessary for the classifier to have the ability to localize each period of the signal objects in CWD-TFI, so that the classifier can utilize the same repeating signal objects over multiple periods in CWD-TFI.

In the literature, there have been several studies on CW LPI radar waveforms. [8] proposed three modified Frank codes (MFC) that allow larger unambiguous range while minimizing the correlation length needed to achieve desired compression gain for target detection. However, [8] concentrate only on signal designing, and does not consider about LPI radar recognition problem. In [9]–[12], the authors attempt to detect or extract parameters of only one modulation scheme (i.e., phase or frequency modulated continuous waveform). [1] extracts features for the input to an MLP by applying principal component analysis (PCA) on the cropped TFI of the twelve CW LPI radar signals (i.e., BPSK, Costas, LFM, Frank, P1, P2, P3, P4, T1, T2, T3 and T4). However, the performance of the LWRT in [1] may be not strong enough for use in practice since the features extracted by the PCA cannot describe the subtle changes in the TFI of the LPI radar signal. Thus, despite the popularity of CW LPI radar, there has not been an LWRT that can classify various CW LPI radar modulation schemes with reasonable performance.

In this paper, we propose an LWRT based on a single shot multi-box detector (SSD) [13] and a supplementary classifier that can classify both PW and CW for all of the twelve LPI radar modulation schemes (i.e., BPSK, Costas, LFM, Frank, P1, P2, P3, P4, T1, T2, T3, and T4). Unlike the CNN classifiers in the existing LWRTs [5], [6], the SSD not only automatically determines the effective features needed to classify the signal objects in CWD-TFI but also, to perform classification, has the ability to localize the regions that contain the same repeating signal objects in CWD-TFI. This ability allows the SSD to perform better than CNN for both PW and CW LPI radar signals. For PW, the SSD does not require exact knowledge of the starting and ending points of the pulse interval. For CW, the SSD performs well even when CWD-TFI contains several consecutive periods of signal objects. However, the SSD is unable to
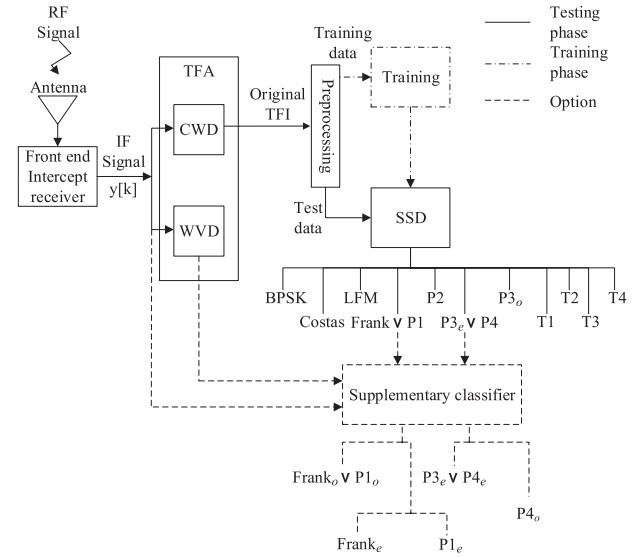

Fig. 1. Block diagram of proposed LWRT.

distinguish certain CW LPI radar signals because of the similarity between their signal objects in CWD-TFI. In these cases, the proposed supplementary classifier is used to fulfill the proposed LWRT.

The contribution of this paper can be summarized as follows. 1) The proposed LWRT based on the SSD and the supplementary classifier can automatically recognize and classify all of the twelve LPI radar modulation schemes [1] in either PW or CW LPI radar waveforms. 2) The proposed LWRT is practically useful compared to existing studies because it achieves exceptional performance even without the condition that the precise pulse interval within the intercepted signal must be exactly known.

Notice that because our approach in the proposed LWRT is supervised learning [14], we need to train the SSD by CWD-TFIs and their corresponding modulation schemes. Therefore, the parameters of the LPI radar waveforms are needed to generate the training data (i.e., CWD-TFIs and their corresponding modulation schemes). Therefore, the proposed LWRT is practical in the case the LWRT system is aware of the parameters range of the LPI radar waveforms, and therefore the SSD can be trained appropriately.

The paper is organized as follows. The proposed LWRT and intercepted LPI radar signal model are presented in Section II. Section III explains the characteristics of the CWD-TFI of the CW LPI radar waveforms and introduces the process used to generate the input to the SSD. Section IV explains the SSD in the proposed LWRT, and the supplementary classifier. Section V shows the simulation results for the proposed LWRT. Finally, conclusions are drawn in Section VI.

II. PROPOSED LWRT

In this section, we provide an overview of the proposed LWRT. Fig. 1 shows the overall operation flow of the proposed LWRT. The receiver intercepts a radio frequency (RF) radar signal, and the intercepted RF signal is amplified by a low noise amplifier (LNA), down-converted to the intermediate frequency (IF)

f_I, and then sampled at $f_s \ (= 1/T_s)$ to produce discrete-time complex samples $y[k]$ as

$$y[k] = x[k] + w[k] = a[k]e^{\alpha\theta[k]} + w[k], \qquad (1)$$

where $x[k]$ represents discrete time complex radar signal samples, $w[k]$ is the complex additive white Gaussian noise (AWGN), k is the sample index, which increases every T_s, $a[k]$ is the non-zero constant signal envelope (i.e., $a[k] = A$), $\alpha = \sqrt{-1}$ is the imaginary unit, and $\theta[k]$ is the instantaneous phase of the intercepted signal. For PW LPI radar waveforms, we assume that the duty cycle $DC(= \tau_{PW}/\tau_{PP})$ is much smaller than one ($DC \ll 1$), where τ_{PW} is the pulse width and τ_{PP} is the pulse period; for the CW LPI radar waveforms, we assume that the duty cycle is one ($DC = 1$). The samples captured by the intercept receiver are fed into the time-frequency analysis (TFA) block to generate the CWD-TFI and WVD-TFI of the signal. Notice that we assume that a set of 2048 consecutive signal samples is collected to use the fast Fourier transform (FFT) for CWD computation and that the 2048 consecutive samples contain at least one complete pulse interval. In the preprocessing block, the CWD-TFI generated in the TFA block is resized to generate input to the SSD, which is the primary classifier of the proposed LWRT. In the training phase depicted by the dot-dashed lines in Fig. 1, the SSD in the proposed LWRT is trained using the output of the preprocessing block as a training data set. The trained SSD classifies both PW and CW LPI radar waveforms of any of the twelve modulation schemes (i.e., BPSK, Costas, LFM, Frank, P1, P2, P3, P4, T1, T2, T3, and T4).

The signal objects in CWD-TFI of CW Frank signal (i.e., the CW LPI radar signal with Frank modulation scheme) are very similar to those of the CW P1 signal. The signal objects in CWD-TFI of the CW P3$_e$ signal (i.e., the CW P3 signal with an even number of frequency steps M) are very similar to those of CW P4 signal. Detailed discussion of the signal objects in CWD-TFI of different modulation schemes is given in Section III. As a result, for the SSD in the proposed LWRT, distinguishing CW Frank from CW P1 and CW P3$_e$ from CW P4 becomes impossible when the CW LPI radar signal samples are captured over multiple pulses with the first sample at an arbitrary point within the earliest pulse interval. On the other hand, the signal objects in CWD-TFI of the CW P3$_o$ signal (i.e., the CW P3 signal with an odd number of frequency steps, M) contain some power spectrum separations, which is different from the signal objects in CWD-TFI of the CW P3$_e$ signal and CW P4 signal. In summary, depending on M (i.e., odd or even), the CW P3 signal results in two different signal objects in CWD-TFI; the CW P3$_o$ signal can be distinguished from the CW P3$_e$ and CW P4 signals using the SSD in the proposed LWRT. Therefore, from the twelve CW LPI radar modulation schemes considered in this paper, there are only eleven distinguishable signal objects in CWD-TFI made from BPSK, Costas, LFM, Frank∨P1 (i.e., Frank or P1), P2, P3$_o$, P3$_e$∨ P4, T1, T2, T3, and T4. However, because of the similarity in the signal objects in CWD-TFI, the SSD in the proposed LWRT can successfully classify only nine signal objects in CWD-TFI, made from BPSK, Costas, LFM, P2, P3$_o$, T1, T2, T3, and T4. And, classifying CW Frank∨P1 into a CW Frank signal or CW P1 signal and classifying CW P3$_e$∨P4 into

a CW P3$_e$ signal or CW P4 signal remain unresolved with the SSD in the proposed LWRT. To classify all of the twelve CW LPI modulation schemes [1] based on their signal objects in CWD-TFI, we propose a supplementary classifier such that when the classification result by the SSD is CW Frank∨P1 or CW P3$_e$∨ P4, the supplementary classifier is activated to determine if the intercepted signal is a CW Frank signal or CW P1 signal or a CW P3$_e$ signal or CW P4 signal, respectively. A detailed description of the supplementary classifier is given in subsection IV-B. Note that the supplementary classifier, depicted by the dashed line in Fig. 1, is needed only when the classification results by SSD are CW Frank∨P1 or CW P3$_e$∨P4.

III. PREPROCESSING TECHNIQUES

In this section, we present the time-frequency analysis (TFA) and describe the simple image processing used for the preprocessing blocks.

A. Time-Frequency Analysis (TFA)

In this subsection, we describe the TFA techniques (i.e., WVD and CWD) used in the proposed LWRT. WVD and CWD are bilinear TFA techniques [1] in which autocorrelation is exploited to obtain robustness against noise. This is the reason that WVD and CWD are used, because the intercepted LPI radar signal often has low SNR. CWD is utilized to generate CWD-TFI, which is the input to the SSD, since CWD behavior can be easily adjusted by changing the value of the scaling parameter [3], which means the time-frequency resolution and the cross-term suppression of CWD can be changed by adjusting the value of the scaling parameter σ. However, as described in Section I and Section II, the SSD is unable to distinguish certain CW LPI radar signals because of the similarity between the signal objects in CWD-TFIs. To classify those signals clearly, we propose a supplementary classifier that utilizes precisely extracted signal parameters. And, because WVD provides the best time-frequency resolution among the bilinear TFA techniques [15], we employ WVD to extract signal parameters for the supplementary classifier. Notice that the role of CWD and WVD are not interchangeable. If CWD is utilized in the parameter extraction function instead of WVD, the accuracy of the extracted parameters should be poor because CWD has lower time-frequency resolution than WVD. On the other hand, if WVD-TFI is used as an input to the SSD, the classification performance should be poor because the cross-terms in the WVD-TFI can conceal the properties of the LPI radar waveforms [16].

1) Wigner-Ville Distribution: The discrete pseudo-WVD is defined as [17]

$$W[\ell, \omega] = 2 \sum_{m=-K+1}^{K-1} h[m]y[\ell+m]h[-m]y^*[\ell-m]e^{-2\alpha\omega m}, \qquad (2)$$

where ℓ is the time index, ω is the angular frequency index, $h[m]$ is a real window function of length $2K - 1$ with $h[0] = 1$ and $K \le (N+1)/2$, and N is the length of the signal $y[k]$ or

$y_a[n]$. In this paper, a rectangular window $h[m]$ of unit amplitude (i.e., $= 1$) is used.

The WVD provides the best time-frequency resolution among all the bilinear TFA techniques [15] . However, the WVD suffers from the cross-term effect, which can conceal important features of the signal [16]. This limitation has motivated the development of certain cross-term suppression techniques, including CWD.

2) Choi-William Distribution: The CWD was developed to address the main drawback of WVD (i.e., the cross-term effect) [18]. It is performed by choosing the kernel function in Cohen's general formula for time-frequency distribution [19],

$$\mathrm{C}[\ell, \omega] = 2 \sum_{\tau=-P/2}^{P/2} e^{-2\alpha\omega\tau} \left[\sum_{\mu=-Q/2}^{Q/2} \frac{1}{\sqrt{4\pi\tau^2/\sigma}} e^{-\frac{\mu^2}{4\tau^2/\sigma}} \right.$$

$$\left. \times\, y[\ell + \mu + \tau] y^*[\ell + \mu - \tau] \right], \tag{3}$$

where $P = Q = 2048$ and σ is the scaling factor. In this paper, $\sigma = 1$ is chosen to maintain the balance between cross-terms reduction and frequency resolution in the CWD results. Note that there are several time-frequency distributions [15], [20] that are better than CWD in term of cross-term suppression and time-frequency resolution, such as smoothed pseudo-WVD (SP-WVD) and modified B distribution (MBD). These TFDs can be utilized instead of CWD to generate the input to the SSD. However, in this paper, to better demonstrate the effectiveness of our contribution (i.e., the SSD and the supplementary classifier), we also utilize CWD-TFI as the existing studies [3]–[6].

Fig. 2 shows the signal objects in CWD-TFI, made from the modulation schemes considered in this paper: BPSK, Costas, LFM, Frank, P1, P2, $P3_o$, $P3_e$, P4, T1, T2, T3, and T4. The parameters used to generate the signals is given in Appendix A. Note that the CW P3 signal results in two different signal objects in CWD-TFI depending on M: CW $P3_o$ and CW $P3_e$.

The signal objects in CWD-TFI of PW LPI radar signals and their description can be found in [1], [5]. The signal objects in CWD-TFI of CW LPI radar with BPSK, Costas, LFM, T1, T2, T3, and T4 modulation schemes are just repetitions of those corresponding PW LPI radar signals, as shown in Fig. 2(a)–2(c), and 2(j)–2(m), respectively. In this paper, we only focus on describing the differences in the signal objects in CWD-TFI of CW LPI radar signals compared to those of PW LPI radar signals.

The first difference occurs between the CW Frank and CW P1 signals. In the case of the PW LPI radar waveforms shown in [5], the PW Frank signal has the biggest phase increments between subcodes (i.e., between the time intervals in which the phase offset remains constant) within the pulse interval. This characteristic results in the separation of the PW Frank signal object in CWD-TFI into two signal clusters. On the other hand, the PW P1 signal has the largest phase increments at both ends (i.e., the beginning and the end) of the pulse interval. This characteristic results in only one signal cluster in CWD-TFI for PW P1 signal. However, for CW Frank signals, as shown in Fig. 2(d), the signal phase at the ending point of a pulse interval has a continuous transition to the signal phase at the starting point of the next
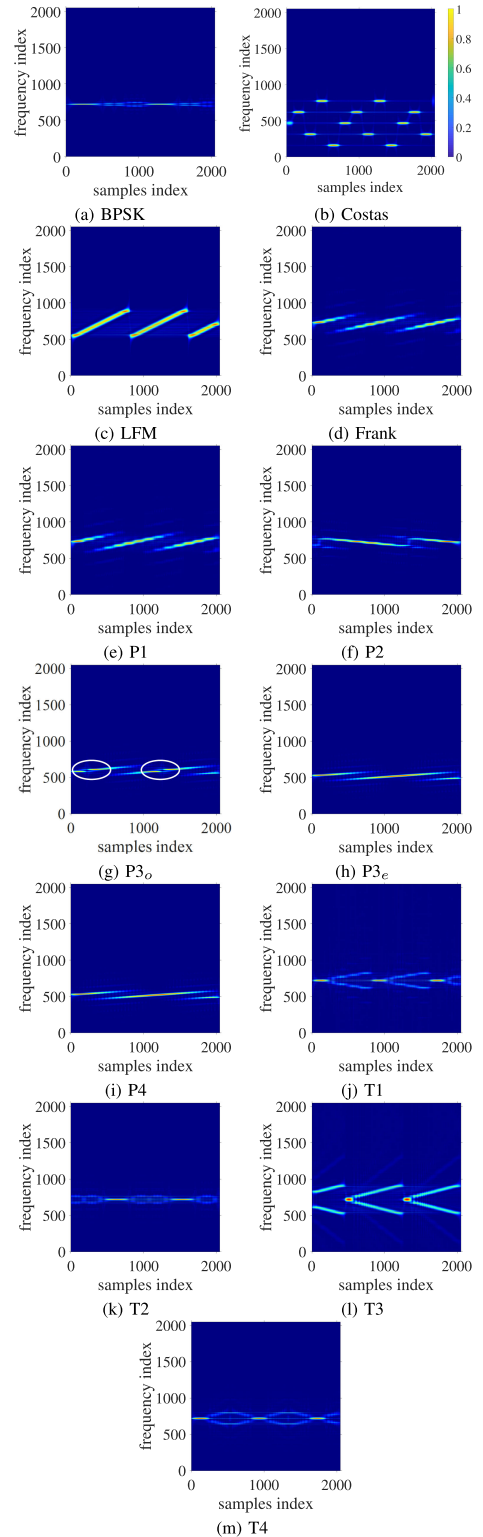

Fig. 2.   CWD-TFIs of CW LPI radar signals over multiple periods.

pulse interval, which results in the signal objects in CWD-TFI being very similar to those of the CW P1 signal, as shown in Fig. 2(e). Therefore, it is impossible to distinguish CW Frank and CW P1 signals based on their signal objects in CWD-TFI. The analysis in the Appendix B shows that when M is odd, the
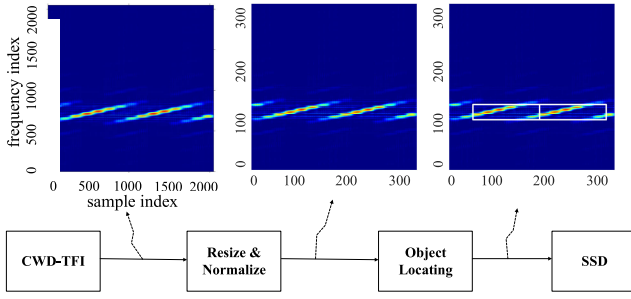
Fig. 3. Image processing for input to the SSD for Frank signal with $f_c = 3fs/16$, $M = 6$, and $N_{cc} = 5$.

CW Frank and CW P1 signals are identical and are just time-delayed versions of each other. As a result, distinguishing CW Frank and CW P1 signals is not possible when M is odd and when the CW LPI radar signal samples are captured over multiple consecutive periods with the first sample at an arbitrary point within the earliest pulse interval. On the other hand, when M is even, CW Frank and CW P1 signals are different even though their signal objects in CWD-TFI are similar. In this case, the supplementary classifier is activated to distinguish CW Frank and CW P1 signals.

The second difference occurs between CW P3 and CW P4 signals, and is very similar to the case of CW Frank and CW P1 signals. When M is even, CW P3 and CW P4 signals are just time-delayed versions of each other. Accordingly, the signal objects in CWD-TFI of CW P3$_e$ are an identical and a time-delayed version to those of the CW P4 signal as shown in Fig. 2(h) and 2(i), respectively. Therefore, distinguishing CW P3$_e$ and CW P4 based on their signal objects in CWD-TFI is not possible. On the other hand, when M is odd, there is a discontinuity in the phase transition from the end of the previous pulse interval to the start of the next pulse interval of the CW P3$_o$ signal. The proof for this claim is included in Appendix C. As a result, there are power spectrum separations in the signal objects in CWD-TFI of CW P3$_o$, as illustrated in the white circles in Fig. 2(g).

Therefore, there are only eleven distinguishable CW signal objects in CWD-TFI (made from BPSK, Costas, LFM, Frank∨P1, P2, P3$_o$, P3$_e$∨P4, T1, T2, T3, and T4). The SSD in the proposed LWRT can distinguish only nine CW signal objects in CWD-TFI (made from BPSK, Costas, LFM, P2, P3$_o$, T1, T2, T3, and T4).

In order to distinguish all of the twelve modulation schemes, we proposed the supplementary classifier to classify CW Frank∨P1 and CW P3$_e$∨P4 into CW Frank or CW P1 and CW P3$_e$ or CW P4 signals, respectively. Details of the supplementary classifier are given in subsection IV-B.

B. Preprocessing: Image Processing

Fig. 3 illustrates the image processing procedure used to produce the input to the SSD in the proposed LWRT. The explanation of the notations f_c, M, and N_{cc} can be found in Table I. To guarantee that the snapshot of the signal contains at least one complete pulse interval, and to exploit the FFT algorithm for

TABLE I
SIGNAL PARAMETERS OF TWELVE MODULATION SCHEMES FOR PW LPI RADAR SIGNALS

Modulation scheme	Parameters	Range
LFM	f_c B N	$U(2f_s/16,\ 3f_s/16)$ $U(f_s/20,\ f_s/10)$ $U[500,\ 1000]$
Costas	FH sequence length {4, 5, 6} f_{min} N	$U(2f_s/80,\ 3f_s/80)$ $U[400,\ 990]$
BPSK	L_c f_c N_{cc}	$\{7,\ 11,\ 13\}$ $U(2f_s/16,\ 3f_s/16)$ $U[10,\ 14]$
Frank , P1	f_c N_{cc} M	$U(2f_s/16,\ 3f_s/16)$ $\{4,\ 5,\ 6\}$ $\{4,\ 5,\ 6\}$
P2	f_c N_{cc} M	$U(2f_s/16,\ 3f_s/16)$ $\{4,\ 5,\ 6\}$ $\{4,\ 6\}$
P3, P4	f_c N_{cc} ρ	$U(2f_s/16,\ 3f_s/16)$ $\{4,\ 5,\ 6\}$ $\{16,\ 25,\ 36\}$
T1, T2	f_c N_g N	$U(2f_s/16,\ 3f_s/16)$ $\{4,\ 5,\ 6\}$ $U[500,\ 1000]$
T3, T4	f_c ΔF N	$U(2f_s/16,\ 3f_s/16)$ $U(f_s/20,\ f_s/10)$ $U[500,\ 1000]$

f_c: center frequency, B: bandwidth, N: number of samples per signal period,

f_{min}: fundamental frequency of the Costas code, L_c: Barker code length,

N_{cc}: number of carrier frequency per subcode, M: number of frequency step,

ρ: number of subcode, N_g: number of segments in a code, ΔF: modulation bandwidth.

fast CWD computation, a set of 2048 consecutive signal samples is collected. The nearest neighbor interpolation (NNI) [21] technique is then used to resize the CWD-TFI of 2048×2048 pixels to 300×300 pixels, which is the input size of the SSD in the proposed LWRT. The locations of the signal objects in CWD-TFI need to be specified by the coordinates of the bounding box and the utilized modulation schemes need to be named, as required for the training of the SSD (but not in the testing phase). Notice that the 2048 consecutive signal samples may contain more than one complete pulse interval, which means CWD-TFI may contain more than one period of signal object. For all periods of signal objects, the locations in CWD-TFI and the modulation schemes should be defined to train the SSD in the proposed LWRT.

IV. CLASSIFIER

In this Section, we introduce the classifiers used in the proposed LWRT. As described in Sections I and II, due to the ability to locate and to recognize signal objects in CWD-TFI, the SSD can distinguish the majority of CW LPI radar modulation schemes, while the performance of the classifying PW LPI radar modulation schemes is similar to better than that of recent LWRTs [3]–[5] developed only for PW LPI radar waveforms. And, with the supplementary classifier, the proposed LWRT
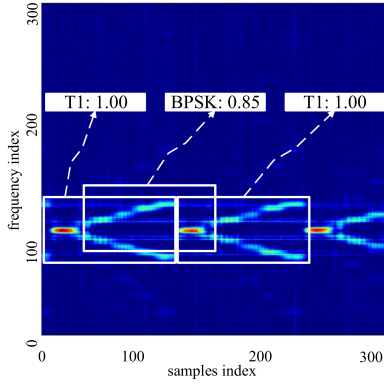
Fig. 4. SSD classification hypotheses of a CW T1 signal with parameters $f_c = 7 \times f_s/40$, $N_g = 6$, and $N = 800$.

Fig. 5. Classification performance of SSD for various network sizes.

guarantees classification of all twelve LPI radar signal modulation schemes.

A. Single Shot Multi-Box Detector (SSD)

In this subsection, we introduce the SSD [13] used in the proposed LWRT. Unlike conventional CNN, which only classifies objects in pictures, SSD can determine the object type and its location in the image. Fig. 4 shows the recognition result of a CW T1 signal (i.e., with parameters $f_c = 7 \times f_s/40$, $N_g = 6$, and $N = 800$) issued by the SSD. The explanation of the notations f_c, N_g, and N can be found in Table I. As can be seen, there are two modulation scheme hypotheses for the signal: 'T1' (with a probability of 1.0) and 'BPSK' (with a probability of 0.85). Since we do not consider a case of combined modulated signals, the classification result becomes 'T1' because it is the highest probability. In existing LWRTs in [3]–[5], it was assumed that CWD-TFIs contain only one pulse interval, and the starting and ending points (i.e., samples) of the pulse interval are precisely known. Nonetheless, this assumption is not realistic because it is difficult in practice to detect the pulse interval exactly when the intercepted signal has low SNR. However, the proposed LWRT can handle cases in which CWD-TFI contains multiple consecutive periods of signal objects, as illustrated in Fig. 4.

While the SSD in the proposed LWRT is based on the SSD300 (i.e., the SSD with input images of the size 300×300 pixels) [13], there are some modifications made to the SSD300 to make it fit the proposed LWRT. The first modification is the number of filters in the convolutional layers. The SSD300 is designed to classify eighty classes in the COCO dataset [22], while the proposed LWRT classifies only twelve modulation schemes of CW or PW LPI radar signals. Consequently, to speed up the classification while not compromising the accuracy, we try to reduce the number of network parameters.

Fig. 5 shows the processing time (which excludes the training time because the training is offline) and the overall classification performance for eleven CW signal objects in CWD-TFI, for the SSD employed in the proposed LWRT with respect to various number of filters at SNR equal to -8 dB, below which the performance of the SSD in the proposed LWRT starts to
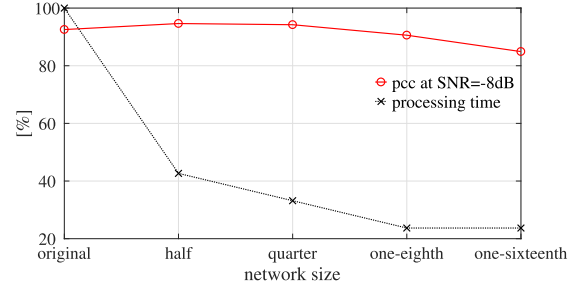
drop dramatically. The processing time of the SSD300 is considered to be 100%. As shown, there is a slight increase in accuracy when the number of filters is reduced by half. In addition, the performance of the half-size-SSD (i.e., SSD with half the number of filters of the SSD300) and quarter-size-SSD are very similar (pcc of 94.61% and 94.23%, respectively), whereas the processing time of the quarter-size-SSD is much smaller than that of half-size-SSD, where pcc means percentage of correct classification. The performance of the one-eighth-size-SSD is much lower than that of the quarter-size-SSD. Thus, compared to the SSD300 in the proposed LWRT, the SSD with a quarter of the number of filters in the convolutional layers is chosen. Note that for each training dataset (i.e., with different number of training data and different parameters used to generate the training data), the hyper-parameter tuning process should be performed to achieve the optimized SSD classifier.

The second modification is in the training phase of the SSD in the proposed LWRT. To achieve more robustness to various input shapes [23], the SSD300 uses data augmentation by horizontally flipping the training image with a probability of 0.5 (i.e., half of the training images are flipped). However, when we flip the CWD-TFI of CW Frank∨P1 horizontally, it looks very similar to that of CW P2 signal, as shown in Fig. 2(d)–2(f), and the trained SSD may not be able to distinguish the CWD-TFIs of the CW Frank∨P1 and CW P2 signals. Therefore, to train the SSD in the proposed LWRT, we do not horizontally flip the CWD-TFI.

The SSD in the proposed LWRT can classify the twelve LPI radar modulation schemes when the DC is less than one, which is the case for PW LPI radar signals. However, when the DC is one (i.e., CW), the signal objects in CWD-TFI of some signals may look similar and cannot be distinguished by the SSD in the proposed LWRT, as discussed in Section II and Section III. To overcome this limitation, we propose a supplementary classifier to further classify those CW LPI radar signals. This supplementary classifier is introduced in the next subsection.

B. Supplementary Classifier

The supplementary classifier is only used for CW LPI radar waveforms and is activated only when the classification results from the SSD in the proposed LWRT are CW Frank∨P1 and CW $P3_e \vee$ P4, to classify CW Frank∨P1 into CW Frank$_o \vee$P1$_o$, CW Frank$_e$, CW P1$_e$, and to classify CW P3$_e \vee$ P4 into CW P3$_e \vee$ P4$_e$, CW P4$_o$ signals. Fig. 6 shows the supplementary classifier, which consists of three functions of parameters extraction,
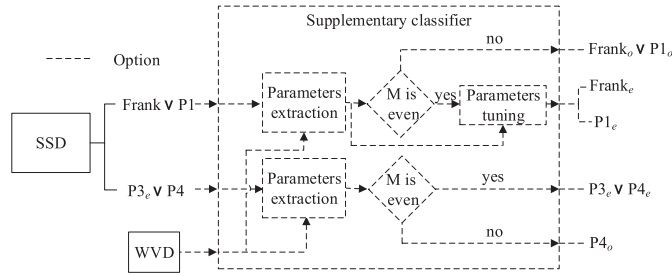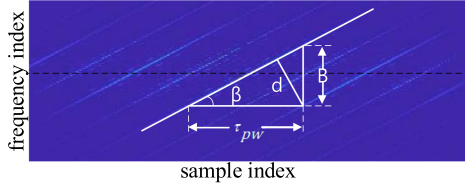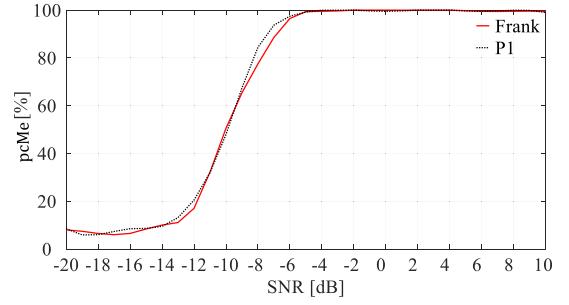
Fig. 6.   Supplementary classifier algorithm flow.

Fig. 7.   Geometry of WVD-TFI used for parameters extraction function [24].

Fig. 8.   Parameters extraction function [24] performance on extracting the number of frequency steps M.

frequency step number (i.e., M) determination, and parameters tuning function.

When the intercepted signal is classified by the SSD in the proposed LWRT as CW Frank∨P1 or CW P3$_e$∨P4, the proposed LWRT extracts signal parameters using WVD and the Radon transform (RT) [24]. As M is estimated using the parameters extraction function, the frequency step determiner decides whether the parameters tuning function should be activated to further classify the signal or not. When the signal is classified by the SSD in the proposed LWRT as CW Frank∨P1 and extracted M is odd, or when the signal is classified as CW CW P3$_e$∨P4 and extracted M is even, no more action is required because the CW Frank$_o$ and CW P3$_e$ signals are just the time-delayed versions of CW P1$_o$ and CW P4$_e$, respectively. The proof of this claim is given in Appendix B. And, when the signal is classified as CW P3$_e$∨ P4 and extracted M is odd, the signal is CW P4$_o$.

When the signal is classified as CW Frank∨P1 and extracted M is even, the parameters tuning function is activated to classify the signal into CW Frank$_e$ or CW P1$_e$. The parameters extraction and parameters tuning functions are described in the next subsections.

1) Parameters Extraction Function: Fig. 7 shows the geometry of WVD-TFI used for the parameters extraction function in [24]. The center frequency f_c can be found from the position of the highest amplitude (intensity) point on the WVD-TFI. Using the RT on the WVD of the signal, the distance d between the intensity lines and the inclination angle β can be estimated. Note that this function requires multiple (i.e., ≥ 2) pulse intervals to make use of the parallel intensity lines. Thus, for the WVD computation, we capture 4096 consecutive signal samples so that there will be at least two complete pulse intervals. Note also that the computation cost for WVD is $\mathcal{O}(N^2 log_2 N)$ [25], which is N times lower than that for CWD (i.e., $\mathcal{O}(N^3 log_2 N)$) [5] . Therefore, doubling the number of intercepted signal samples (i.e., 4096 instead of 2048) for WVD computation causes only a slight increase in the overall computation cost of the proposed

LWRT. The signal bandwidth B and pulse width τ_{PW} are then calculated using the trigonometric relations. The cycle number of the carrier frequency per subcode N_{cc} and number of frequency steps M are then calculated from B and τ_{PW}, using the formulas:

$$N_{cc} = f_c/B, \qquad (4)$$
$$M^2 = B \times \tau_{PW}. \qquad (5)$$

Details of the function can be found in [24].

2) Parameters Tuning Function: The Parameters tuning function is optional and activated only when the classification result by SSD in the proposed LWRT is Frank∨P1 and the extracted number of frequency steps (i.e., M) is even. Therefore, estimating M correctly is important because it decides the activation of the parameters tuning function.

Fig. 8 shows the performance of the parameters extraction function in subsection IV-B1 on extracting M. As can be seen, the percentage of correct M extractions (pcMe) for CW Frank and CW P1 signals starts to decrease dramatically at SNR -8 dB and is highly reliable at SNR ≥ -6 dB. Therefore, the proper activation of the parameters tuning function is guaranteed for SNR ≥ -6 dB.

Given that M of the CW Frank∨P1 signal is even and extracted correctly, the parameters tuning function is activated to classify Frank∨P1 (i.e., with even M) into Frank$_e$ and P1$_e$ signals. With the extracted parameters (i.e., f_c, N_{cc}) from parameters extraction function as the input, the parameters tuning function performs the following steps:

1) Set the parameters tuning range: $\pm 5\%$ of f_c with a step size of 0.05%, and ± 1 of N_{cc} with a step size of 1.
2) Generate Frank$_e$ replicas and P1$_e$ replicas using the extracted M as well as f_c and N_{cc} values defined in step 1. Note that one pulse interval is used for the replicas.
3) Perform cross-correlations between the intercepted signal and each of the Frank$_e$ replicas and between the intercepted signal and each of the P1$_e$ replicas.
4) Let p_{Fr} and p_{P1} be the maximum peak values of the cross-correlation between the intercepted signal and the Frank$_e$ replicas and that between the intercepted signal and the P1$_e$ replicas, respectively. When $p_{Fr} > p_{P1}$, the signal is classified as Frank$_e$; otherwise, it is classified as P1$_e$.
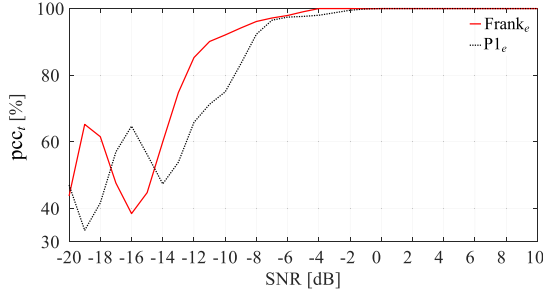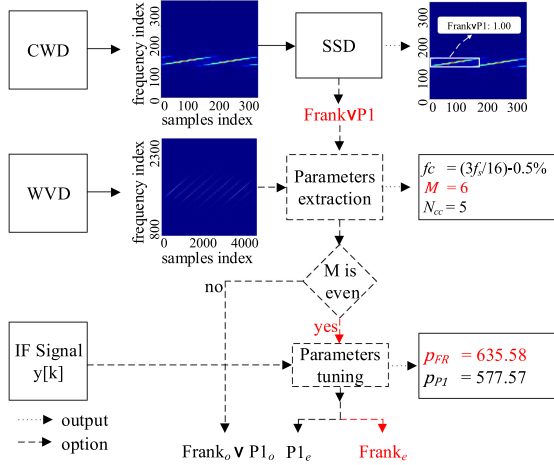
Fig. 9.   Parameters tunning function performance.

Fig. 10.   Operation of overall system for Frank signal input with $f_c = 3fs/16$, $M = 6$, and $N_{cc} = 5$.

Fig. 11.   Cumulative distribution function (CDF) of the overall system processing time.

V. SIMULATION RESULTS

In this section, we compare the performance of the proposed LWRT and that of LWRT in [4]–[6] for PW LPI radar waveforms. In addition, the performances of the proposed LWRT and that of LWRT in [1] for CW LPI radar waveforms are also compared.

A. Performance Comparison to LWRT in [4]–[6] for PW LPI Radar Waveforms

The first simulation is a performance comparison between the proposed LWRT and the LWRTs introduced in [4]–[6] for PW LPI radar waveforms. There are twelve modulation schemes considered in this simulation: BPSK, Costas, LFM, Frank, P1, P2, P3, P4, T1, T2, T3, and T4. The LWRT in [4]–[6] assumes that the signal is captured from the beginning to the end of a single pulse interval. However, for the proposed LWRT, the pulse interval can be anywhere within the 2048 consecutive samples, which shows that the proposed LWRT can be more practical.

Table I shows the signal parameters used to compare the proposed LWRT with the LWRT in [4]–[6] for PW LPI radar waveforms, where $U(.)$ denotes the uniform distribution of a rational number, and $U[.]$ represents the uniform distribution of an integer. The signal parameters are set to make sure that at least one complete pulse interval is contained within the 2048 consecutive samples of the intercepted signal. To train the SSD in the proposed LWRT, we generate 32,400 signals for twelve modulation schemes, such that each modulation scheme has 2,700 signals with SNR ranging from 10 dB to -6 dB and a step size of 2 dB. We divide the 32,400 signals into a training set of 25,920 signals (80% of the total) and a validation set of 6,480 signals (20% of the total). For the test data, we generate 38,400 signals for twelve modulation schemes (i.e., 3,200 signals for each modulation scheme with SNR ranging from 10 dB to -20 dB and a step size of 2 dB).

Fig. 9 shows the percentage of correct classification (pcc) of the parameters tuning function, denoted as pcc_t, used to classify CW Frank_e and CW P1_e signals given that M is even and extracted correctly. As shown, the parameters tuning function is highly reliable for an intercepted signal with SNR ≥ -6 dB. And, around SNR $= -8$ dB, pcc_t starts to drop dramatically, which means the parameters tuning function can be unreliable.

Fig. 10 demonstrates the operation of the overall system when the intercepted signal is CW Frank signal with $f_c = 3fs/16$, $M = 6$, and $N_{cc} = 5$. As can be seen, after the SSD successfully classify the intercepted signal as Frank∨P1, the parameters extraction and the parameters tuning functions further classify the signal into Frank_e signal.

Fig. 11 illustrates the cumulative distribution function (CDF) of the overall system processing time. The computation costs for CWD and WVD are $\mathcal{O}(N^3 log_2 N)$ and $\mathcal{O}(N^2 log_2 N)$, respectively [5], [25]. Note that for the SSD, we only consider processing time in the testing phase because the training phase is off-line. As shown, CWD computation and parameters extraction function account for more than 90% of the total computation cost of the system. Therefore, increasing the speed for CWD computation and parameter extraction function is a suitable approach to decrease the overall computation cost of the system.
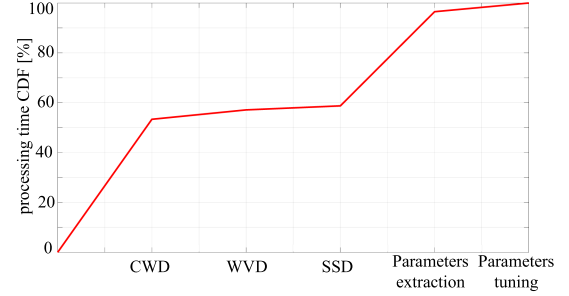
Fig. 12 shows the classification performance of the proposed LWRT and the LWRT in [4]–[6]. As shown, the LWRT in [4] only consider 8 modulation schemes, such BPSK, Costas, LFM, Frank, P1, P2, P3, and P4. Similarly, the LWRT in [6] only consider 8 modulation schemes, such as BPSK, Costas, LFM, Frank, T1, T2, T3, and T4. Moreover, the simulation result of the LWRT in [4] and [6] are available only for SNR ≥ -8 dB and SNR ≥ -4 dB, respectively. As shown in Fig. 12(a), the proposed LWRT achieves an overall performance similar to the
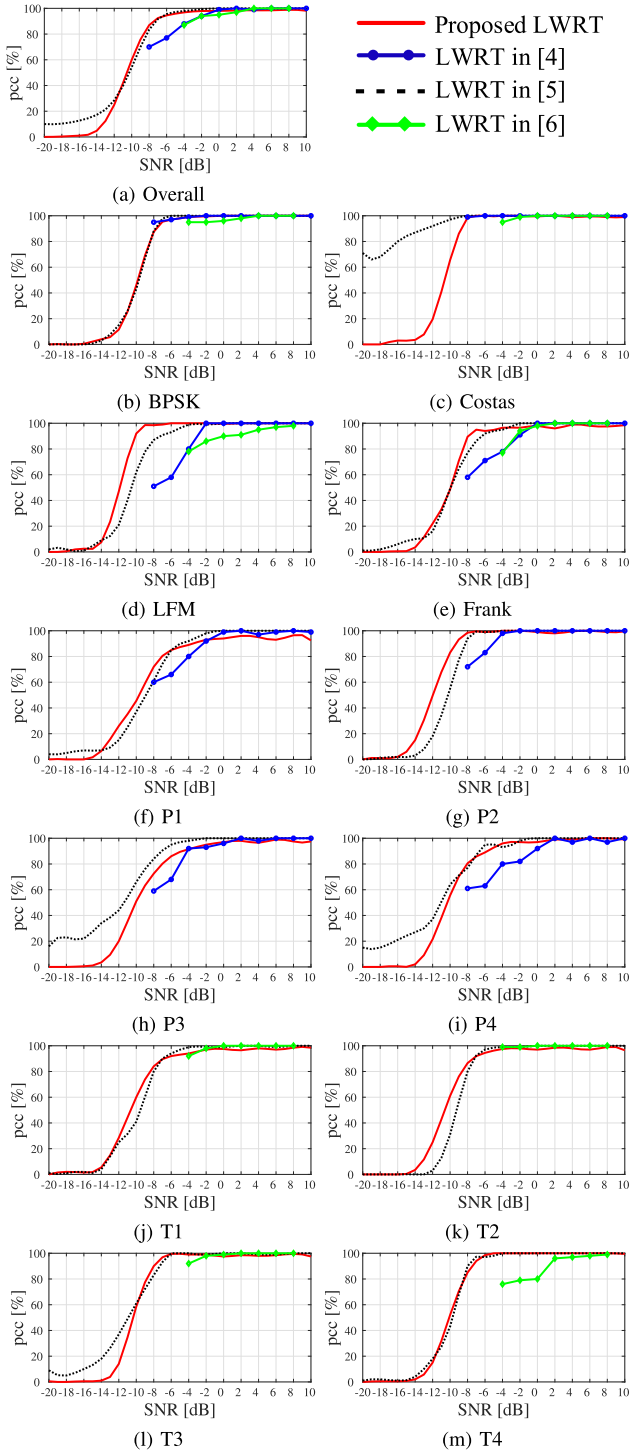
Fig. 12.   Performance comparison with LWRT in [4]–[6] for PW LPI radar signals.

of the proposed LWRT. However, for this range of SNR, both LWRTs are unreliable because the pcc values of both LWRTs are below 30%. As shown in Fig. 12(b)–12(m), for the twelve PW LPI radar waveforms, both LWRTs achieve pcc values of more than 95% for SNR ≥ around 6 dB, below which the pcc starts to decrease dramatically. While the performance of the proposed LWRT for each signal is similar to that of the LWRT in [5], with absolute difference of less than 20%, there is a noticeable performance difference between the two LWRTs for the Costas signal. As shown in Fig. 12(c), [5] achieves a much higher pcc for the Costas signal at low SNR (i.e., SNR ≤ −12 dB) than does the proposed LWRT. However, for this range of SNR, the classification of the LWRT in [5] is unreliable because the intercepted signals are too noisy. In fact, the high pcc level for the Costas signal at the lower SNR is caused by the LWRT in [5] classifying most of the noisy signals as Costas signals.

Note that there are slight imperfections in the classification performance of the proposed LWRT for polyphase signals, such as Frank, P1, P3, and P4 at some high SNR levels, as shown in Fig. 12(e)–12(f) and 12(h)–12(i). This happens when Frank and P1 signals are misclassified as P3 and P4 signals, and vice versa, because the intercepted signals contain only one pulse interval within a much longer signal snapshot, resulting in a small signal object on large CWD-TFI; it then becomes difficult for the CWD-TFI to express the subtle shapes of the signal objects in CWD-TFI, which is the key to distinguishing polyphase signals [5].

Table II is the confusion matrix for SNR = {10, 4, −2, −8, −14, −20} dB of the proposed LWRT classifying PW LPI radar waveforms. The columns show the real modulation schemes, whereas the rows express the classification results by the SSD. As can be seen, at SNR = −8 dB when the performance of the proposed LWRT starts to decrease dramatically, BPSK, Frank, and P1 are misclassified as T2, P3, and P4, respectively. It is because of the similarities in the CWD-TFIs of different modulation schemes as described in [5]. For lower SNR level, most signals are classified as 'No signal', because the CWD-TFIs are too noisy.

B. Discussion on Classification Performance of Existing LWRTs for CW LPI Radar Waveforms

In this subsection, we discuss how the existing LWRTs perform for CW LPI radar waveforms.

In the literature, up to present there has been only one LWRT designed to classify CW LPI radar waveforms. In [1], the authors apply PCA to cropped TFIs to extract statistical features for input to an MLP in order to distinguish twelve CW LPI radar signals (i.e. BPSK, Costas, LFM, Frank, P1, P2, P3, P4, T1, T2, T3 and T4). However, because the features extracted by the PCA may not describe the subtle shapes on the TFI of the LPI radar signals, the pcc of the LWRT in [1] is only about 40% for polyphase signals (i.e., Frank, P1, P2, P3, and P4) and about 60% for polytime signals (i.e., T1, T2, T3, and T4), even at high SNR of 10 dB, which is not acceptable for practical applications.

On the other hand, there have been two different approaches of using LWRTs to classify PW LPI radar waveforms that might

LWRT in [5], and higher than the LWRTs in [4], [6] for SNR greater than −12 dB, where for the proposed LWRT it is not assumed that the position of the pulse interval (i.e., the beginning and ending sample points of the pulse) is known precisely. This testifies that the proposed LWRT is practically useful. For SNR ≤ −12 dB, the overall pcc of the LWRT in [5] is higher than that

TABLE II
CONFUSION MATRIX FOR $\mathbf{SNR} = \{10, 4, -2, -8, -14, -20\}$ **dB** OF THE PROPOSED LWRT CLASSIFYING PW LPI RADAR WAVEFORMS

Modulation schemes	BPSK	Costas	LFM	Frank	P1	P2	P3	P4	T1	T2	T3	T4	No signal
BPSK	200/200/199 175/8/0	0/0/0 0/2/1	0/0/0 0/0/0	0/0/0 0/1/0	0/0/0 0/0/0	0/0/0 1/0/0	0/0/0 0/0/0	0/0/0 0/0/0	0/0/0 4/7/0	0/0/1 17/11/0	0/0/0 0/0/1	0/0/0 0/2/0	0/0/0 3/169/198
Costas	0/0/0 0/0/0	198/198/200 197/7/0	0/0/0 0/0/0	0/0/0 0/0/0	0/0/0 0/0/0	0/0/0 0/0/0	0/0/0 0/0/0	0/0/0 0/0/0	0/0/0 0/0/0	0/0/0 0/0/0	0/0/0 0/1/1	0/0/0 0/0/0	2/2/0 3/192/199
LFM	0/0/0 0/0/0	0/0/0 0/3/0	200/200/200 197/15/0	0/0/0 0/0/0	0/0/0 1/6/0	0/0/0 0/0/0	0/0/0 0/0/0	0/0/0 0/3/0	0/0/0 0/7/0	0/0/0 0/2/0	0/0/0 0/12/0	0/0/0 1/22/0	0/0/0 1/130/200
Frank	0/0/0 0/0/0	0/0/0 0/3/0	0/0/0 0/0/0	197/198/193 179/7/0	0/0/0 2/5/0	0/0/0 0/1/0	0/0/1 10/1/0	0/0/0 1/2/0	0/0/0 5/10/2	0/0/0 0/8/1	0/0/0 0/0/1	0/0/0 0/3/0	3/2/6 3/160/196
P1	0/0/0 0/1/0	0/0/0 0/3/1	0/0/0 3/1/0	0/0/0 1/1/0	185/190/186 144/13/0	0/0/0 0/0/0	0/0/0 0/0/0	0/0/2 41/3/0	0/0/0 1/6/0	0/0/0 1/10/0	0/0/0 0/2/0	0/0/0 3/7/0	15/10/12 6/153/199
P2	0/0/0 0/0/0	0/0/0 0/0/0	0/0/0 0/0/0	0/0/0 0/0/0	0/0/0 0/0/0	199/199/200 197/30/0	0/0/0 0/0/0	0/0/0 0/0/0	0/0/0 0/10/0	0/0/0 0/11/0	0/0/0 1/2/0	0/0/0 0/4/0	1/1/0 2/143/200
P3	0/0/0 0/0/0	0/0/0 0/1/0	0/0/0 0/0/0	0/2/8 32/5/0	0/0/0 0/2/0	0/0/0 1/0/0	195/193/190 145/7/0	0/0/0 10/4/0	0/0/0 0/5/0	0/0/0 1/8/0	0/0/0 0/0/0	0/0/0 1/2/0	5/5/2 10/166/200
P4	0/0/0 0/0/0	0/0/0 0/3/0	0/0/1 8/1/0	0/0/0 1/4/0	0/0/0 19/8/0	0/0/0 0/0/0	0/0/0 0/0/0	198/198/194 161/4/0	0/0/0 0/5/0	0/0/0 0/20/0	0/0/0 0/4/1	0/0/0 2/12/0	2/2/5 9/139/199
T1	0/0/0 1/2/0	0/0/0 0/1/0	0/0/0 0/1/0	0/0/0 5/0/0	0/0/0 0/0/0	0/0/0 3/1/0	0/0/0 0/0/0	0/0/0 0/0/0	197/196/194 168/11/0	2/2/5 18/11/0	0/0/1 3/4/1	0/0/0 0/0/0	1/2/0 2/175/199
T2	0/0/0 4/2/0	0/0/0 0/3/0	0/0/0 0/0/0	0/0/0 0/0/0	0/0/0 4/0/0	0/0/0 2/2/0	0/0/0 0/0/0	0/0/0 0/0/0	0/0/0 1/3/1	193/196/196 173/7/0	0/0/0 0/1/0	7/4/4 11/3/1	5/5/0 5/179/198
T3	0/0/0 0/0/0	0/0/0 0/0/1	0/0/0 2/0/0	0/0/0 0/0/0	0/0/0 0/0/0	0/0/0 0/1/0	0/0/0 0/0/0	0/0/0 1/0/0	0/0/0 2/5/0	0/0/0 0/0/0	195/196/198 180/2/1	0/0/0 3/2/1	5/4/2 12/190/197
T4	0/0/0 0/0/0	0/0/0 1/0/1	0/0/0 2/0/0	0/0/0 0/0/0	0/0/0 0/0/0	0/0/0 1/0/0	0/0/0 3/3/0	0/0/0 0/0/0	0/0/0 0/0/0	0/0/0 4/1/2	0/0/0 2/4/0	199/200/200 170/4/0	1/0/0 15/188/197

be utilized for the classification of CW LPI radar waveforms. The first LWRT approach is based on neural networks such as MLP [3] or RNN [4] and utilizes features extracted from PW LPI radar signals. The second LWRT approach is based on CNN and uses CWD-TFIs of PW LPI radar signals [5], [6]. However, both approaches may fail to achieve an acceptable classification performance for CW LPI radar waveforms because of their limitations, as described in the following.

The LWRTs in [3], [4] have three critical limitations in their application to CW LPI radar signals; first, those LWRTs use certain features that are useful to distinguish PW LPI radar waveforms but not to distinguish CW LPI radar waveforms. For example, both of the LWRTs utilize the number of signal clusters in the CWD-TFI to distinguish PW Frank and PW P3 signals from PW P1 and PW P4 signals. However, this feature (i.e., the number of signal clusters in the CWD-TFI) is not effective on CW LPI radar signals because the intercepted signals (i.e., Frank, P1, P3, and P4) may contain multiple pulse intervals, resulting in multiple signal clusters in the CWD-TFI of CW Frank, CW P1, CW P3, and CW P4 signals. Therefore, it may be difficult for the LWRTs in [3], [4], relying on this feature, to distinguish CW Frank signals from CW P1 signals and to distinguish CW P3 signals from CW P4 signals. Second, since the LWRTs in [3], [4] do not consider polytime signals (i.e., T1, T2, T3, and T4), the features suitable to distinguish those signals have not been studied. Therefore, the expected classification performance of the LWRT in [3], [4] for polytime signals should be poor. Third, even though the LWRTs in [3], [4] can work for other signals (i.e., BPSK, Costas, and LFM), there is about 20% (or larger) performance degradation at SNR ≤ -3 dB in the presence of residual frequency that can corrupt the features extracted from the complex envelope (CE) of the intercepted signals [3].

On the other hand, the LWRTs based on CNN and CWD-TFI of the PW LPI radar signals also have limitations in classifying CW LPI radar signals. First, due to the localization problem, CNN only performs well for image classification but not for object detection in general [26]. However, since the CWD-TFIs of CW LPI radar signals may contain multiple consecutive periods of signal objects, it is necessary for the classifier to have the ability to localize each period of the signal objects in CWD-TFI

in order to recognize signal objects with a higher pcc. Therefore, the proposed LWRT exploits the SSD to achieve better classification performance for CW LPI radar waveforms. However, the SSD alone is unable to distinguish some of the CW LPI radar signals due to similarities in the signal objects in CWD-TFI. For example, as discussed in the previous sections, signal objects in CWD-TFI of a CW Frank signal are very similar to those of a CW P1 signal; also, the signal objects in CWD-TFI of a CW $P3_e$ signal are very similar to those of a CW P4 signal. This is the reason we propose the supplementary classifier to distinguish all of the twelve modulation schemes (i.e. BPSK, Costas, LFM, Frank, P1, P2, P3, P4, T1, T2, T3 and T4) defined in [5]. The classification performance of the proposed LWRT with the SSD and the supplementary classifier for CW LPI radar waveforms is given in the next subsection.

C. Performance Comparison to LWRT in [1] for CW LPI Radar Waveforms

The second simulation is used to compare the performance of the proposed LWRT and the LWRT in [1] for CW LPI radar waveforms. The number of signals generated for training, validating, and testing, and the signals parameters are similar to that for the simulation of PW LPI radar waveforms in subsection V-A and Table I. However, there are some modifications due to the similarity between the signal objects in CWD-TFI of different modulation schemes, as described in Section III; First, CW Frank and CW P1 signals have the same signal objects in CWD-TFI (i.e., these two signals are classified as CW Frank∨P1). CW $P3_e$ and CW P4 signals have the same signal objects in CWD-TFI as well (i.e., these two signals are classified as CW $P3_e\vee$ P4). Second, CW $P3_o$ signals have signal objects in CWD-TFI that are different from those of other signals. As a summary, for the SSD in the proposed LWRT, there are eleven signal objects in CWD-TFI, made from BPSK, Costas, LFM, Frank∨P1, P2, $P3_o$, $P3_e\vee$ P4, T1, T2, T3, and T4.

Fig. 13 shows the performances of the proposed LWRT and LWRT in [1] for CW LPI radar signals. As can be seen, the proposed LWRT outperforms the LWRT in [1] because of the reasons as discussed in subsection V-B. The classification
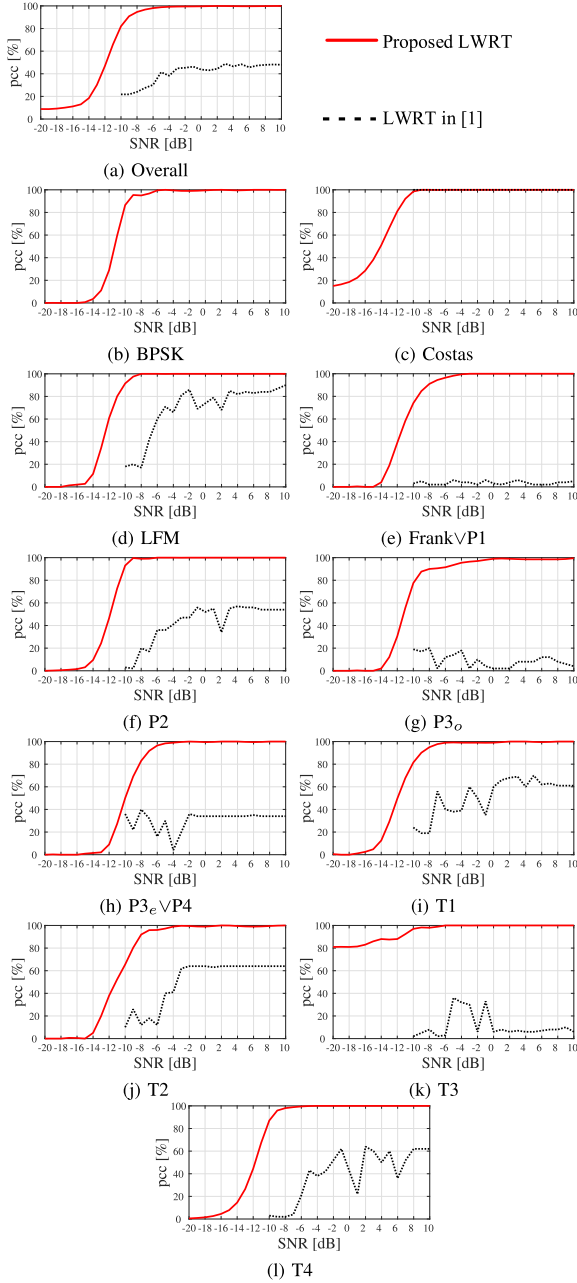
Fig. 13. Performance comparison of proposed LWRT and the LWRT in [1] for CW LPI radar signals.

performances of the proposed LWRT for CW Costas and CW LFM are the best among the LPI radar signals, reaching the saturation points (i.e., an SNR above which the pcc of the proposed LWRT is stable and higher than 99%) at around SNR = −10 dB and SNR = −8 dB, as shown in Fig. 13(c) and Fig. 13(d), respectively. The classification performances of BPSK and polytime (i.e., T1, T2, T3, and T4) signals reach the saturation point at around SNR = −6 dB, as shown in Fig. 13(b) and 13(i)–13(l), respectively. The polyphase signals, such as Frank∨P1, P2, P3$_o$, and P3$_e$ ∨ P4, have the worst classification performance, reaching their saturation points at around SNR = −2 dB to SNR = −4 dB as shown in Fig. 13(e)–13(h), respectively. This

is because the signal objects in CWD-TFI of the BPSK, Costas, LFM, and polytime signals are more distinctive than those of the polyphase signals.

Notice also that the classification performance for CW polyphase signals such as Frank∨P1, P2, P3$_o$, and P3$_e$ ∨ P4 at high SNR levels, as shown in Fig. 13(e), 13(g), and 13(h), are better than that for PW polyphase signals shown in Fig. 12(e)–12(i), respectively. This is because the CWD-TFI of CW LPI radar signals may contain multiple periods of signal object, while that of PW LPI radar signals has only a single period of signal object. In fact, multiple consecutive periods of signal objects in the training CWD-TFIs provide the SSD in the proposed LWRT with more training information. This results in an approximately 2 dB improvement in the overall classification performance for CW signals, as shown in Fig. 13(a), compared to that of the PW signals in Fig. 12(a).

Table III is the confusion matrix for **SNR** = $\{10, 4, −2, −8, −14, −20\}$ dB of the proposed LWRT classifying CW LPI radar waveforms. As can be seen, for SNR ≤ −14 dB, most signals are classified as T3, which means the SSD in the proposed LWRT has a bias toward T3 signal in the extreme noisy cases, explaining the high classification result for T3 signal with low SNR as in Fig. 13(k).

Note also that the classification performance shown in Fig. 13 contains two ambiguous signal objects in CWD-TFI: CW Frank∨P1 and CW P3$_e$∨P4; in fact, Fig. 13(e) and Fig. 13(h) show the performance when the classification results are Frank∨P1 and CW P3$_e$∨P4, respectively. As discussed in subsection IV-B, CW Frank∨P1 can be classified into CW Frank$_o$ ∨ P1$_o$, CW Frank$_e$, and CW P1$_e$; similarly, CW P3$_e$∨P4 can be classified into CW P3$_e$∨P4$_e$ and P4$_o$, which are possible with the proposed supplementary classifier. Based on the supplementary classifier described in subsection IV-B and depicted in Fig. 6, the pcc values of the signals are calculated by the probability chain rule:

$$\text{pcc}_{\text{Frank}_o\vee\text{P1}_o} = \text{pcc}_{\text{Frank}\vee\text{P1}} \times \text{pcMe}, \tag{6}$$

$$\text{pcc}_{\text{Frank}_e} = \text{pcc}_{\text{Frank}\vee\text{P1}} \times \text{pcMe} \times \text{pcc}_{t_{Fr}}, \tag{7}$$

$$\text{pcc}_{\text{P1}_e} = \text{pcc}_{\text{Frank}\vee\text{P1}} \times \text{pcMe} \times \text{pcc}_{t_{P1}}, \tag{8}$$

$$\text{pcc}_{\text{P4}_o} = \text{pcc}_{\text{P3}_e\vee\text{P4}_e} = \text{pcc}_{\text{P3}_e\vee\text{P4}} \times \text{pcMe}, \tag{9}$$

where $\text{pcc}_{\text{Frank}_o\vee\text{P1}_o}$, $\text{pcc}_{\text{Frank}_e}$, pcc_{P1_e}, pcc_{P4_o} and $\text{pcc}_{\text{P3}_e\vee\text{P4}_e}$ are the overall pcc of the proposed LWRT for CW Frank$_o$∨ P1$_o$, CW Frank$_e$, CW P1$_e$, CW P4$_o$, and CW P3$_e$∨P4$_e$ signals, respectively. $\text{pcc}_{\text{Frank}\vee\text{P1}}$ and $\text{pcc}_{\text{P3}_e\vee\text{P4}}$ are the pcc of the SSD in the proposed LWRT for CW Frank∨P1 and CW P3$_e$∨P4 signals, respectively. $\text{pcc}_{t_{Fr}}$ and $\text{pcc}_{t_{P1}}$ are the pcc values of the parameters tuning function for CW Frank and CW P1 signals, respectively, given that M is even and extracted correctly.

The detailed classification performance of the proposed LWRT for CW polyphase signals except CW P2 and CW P3$_o$ signals is given in Fig. 14. Note that for illustrational simplicity the result for CW P3$_e$ ∨ P4$_e$ is not shown since the performance is identical to that of the CW P4$_o$ signal. As shown in Fig. 13(e) and 13(h), for SNR ≥ −6 dB, there is a slight performance degradation compared to pcc$_{\text{Frank}\vee\text{P1}}$ and pcc$_{\text{P3}_e\vee\text{P4}}$ because pcMe and

TABLE III
CONFUSION MATRIX FOR $\mathbf{SNR} = \{\,10, 4, -2, -8, -14, -20\}$ dB OF THE PROPOSED LWRT CLASSIFYING CW LPI RADAR WAVEFORMS

Modulation schemes	BPSK	Costas	LFM	Frank∨P1	P2	P3$_o$	P3$_e$∨P4	T1	T2	T3	T4	No signal
BPSK	200/199/198 190/7/0	0/0/0 0/2/19	0/0/0 0/0/0	0/0/0 0/1/0	0/0/0 1/3/0	0/0/0 0/0/0	0/0/0 0/0/0	0/0/0 0/17/0	0/1/2 8/13/0	0/0/0 0/33/145	0/0/0 0/11/1	0/0/0 1/113/35
Costas	0/0/0 0/0/0	200/200/200 200/102/30	0/0/0 0/0/0	0/0/0 0/0/0	0/0/0 0/0/0	0/0/0 0/0/0	0/0/0 0/0/0	0/0/0 0/4/3	0/0/0 0/0/0	0/0/0 0/75/135	0/0/0 0/3/2	0/0/0 0/16/30
LFM	0/0/0 0/0/0	0/0/0 0/3/15	200/200/200 200/23/0	0/0/0 0/1/0	0/0/0 0/0/0	0/0/0 0/0/0	0/0/0 0/0/0	0/0/0 0/12/1	0/0/0 0/0/0	0/0/0 0/100/149	0/0/0 0/43/3	0/0/0 0/18/32
Frank∨P1	0/0/0 0/0/0	0/0/0 0/3/8	0/0/0 0/1/0	200/200/200 182/8/0	0/0/0 0/0/0	0/0/0 2/4/0	0/0/0 13/1/0	0/0/0 0/21/0	0/0/0 0/13/0	0/0/0 0/41/150	0/0/0 0/24/3	0/0/0 3/84/39
P2	0/0/0 0/0/0	0/0/0 0/2/12	0/0/0 0/0/0	0/0/0 0/0/0	200/200/200 198/19/0	0/0/0 0/0/0	0/0/0 0/0/0	0/0/0 0/22/4	0/0/0 2/11/0	0/0/0 0/52/150	0/0/0 0/11/1	0/0/0 0/83/33
P3$_o$	0/0/0 0/0/0	0/0/0 0/3/20	0/1/6 2/1/0	1/2/0 16/4/0	0/0/0 0/0/0	199/197/194 180/4/0	0/0/0 2/0/0	0/0/0 0/32/1	0/0/0 0/5/0	0/0/0 0/53/149	0/0/0 0/25/0	0/0/0 0/73/30
P3$_e$∨P4	0/0/0 0/0/0	0/0/0 0/0/15	0/0/0 0/2/0	0/0/0 28/9/0	0/0/0 0/0/0	0/0/0 2/8/0	200/200/200 166/3/0	0/0/0 0/18/2	0/0/0 0/5/0	0/0/0 0/59/152	0/0/0 0/20/0	0/0/0 4/76/31
T1	0/0/0 0/0/0	0/0/0 0/6/11	0/0/0 0/0/0	0/0/0 0/0/0	0/0/0 1/0/0	0/0/0 0/0/0	0/0/0 0/0/0	200/200/198 190/25/0	0/0/0 4/4/0	0/0/2 4/100/149	0/0/0 0/15/0	0/0/0 1/50/39
T2	0/1/1 9/6/0	0/0/0 0/9/14	0/0/0 0/0/0	0/0/0 0/0/0	0/0/0 1/1/0	0/0/0 0/0/0	0/0/0 0/0/0	0/0/0 4/26/3	200/199/199 184/10/0	0/0/0 0/58/144	0/0/0 2/19/1	0/0/0 0/71/38
T3	0/0/0 0/0/0	0/0/0 1/10/18	0/0/0 0/0/0	0/0/0 0/0/0	0/0/0 0/0/0	0/0/0 0/0/0	0/0/0 0/0/0	0/0/0 3/5/0	0/0/0 0/0/0	200/200/200 196/176/162	0/0/0 0/0/3	0/0/0 0/9/17
T4	0/0/0 0/0/0	0/0/0 1/8/11	0/0/0 0/0/0	0/0/0 0/0/0	0/0/0 0/0/0	0/0/0 0/0/0	0/0/0 0/0/0	0/0/0 1/6/0	0/0/0 2/0/0	0/0/0 0/130/157	200/200/200 196/29/1	0/0/0 0/27/31

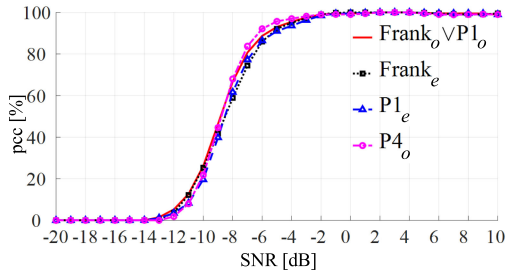Fig. 14. Performance of proposed LWRT on CW polyphase signals except for P2 and P3$_o$.

pcc_t become very close to one for SNR ≥ -6 dB. Thus, the supplementary classifier successfully classifies CW Frank∨P1 and CW P3$_e$∨P4 into CW Frank$_o$∨P1$_o$, CW Frank$_e$, CW P1$_e$ and CW P3$_e$∨P4$_e$, CW P4$_o$ signals, respectively. As a result, the proposed LWRT can successfully classify all twelve modulation schemes considered in this paper, such as BPSK, Costas, LFM, Frank, P1, P2, P3, P4, T1, T2, T3, and T4.

VI. CONCLUSION

In this paper, we have proposed an LWRT based on SSD and a supplementary classifier. It has been demonstrated that the proposed LWRT can work for both PW and CW LPI radar waveforms without the condition of prior knowledge of the beginning and ending sample points of the captured pulse interval. For PW LPI radar waveforms, the proposed LWRT has demonstrated in Monte Carlo simulations that it can achieve classification performance similar to that of the recent LWRT in [5], which is one of the best performance techniques. This is even though the proposed LWRT does not require the condition used in existing studies. For CW LPI radar waveforms, by exploiting the SSD and the proposed supplementary classifier, the proposed LWRT can distinguish all twelve modulation schemes with exceptional performance, which is impossible for the existing LWRTs due to similarities in signal objects in CWD-TFI. In fact, the overall classification performance of the proposed LWRT for CW LPI radar waveforms is even about 2 dB higher than that for PW LPI radar waveforms. Therefore, by achieving extraordinary

classification performance for general LPI radar waveforms (i.e., PW and CW) modulated with any of the twelve modulation schemes, the proposed LWRT is useful for LPI radar classification in practice, i.e., in real electronic warfare.

APPENDIX A
PARAMETERS USED TO GENERATE THE SIGNALS IN FIG. 2

Table IV shows the parameter used to generate the signals in Fig. 2.

TABLE IV
PARAMETERS USED TO GENERATE THE SIGNALS IN FIG. 2

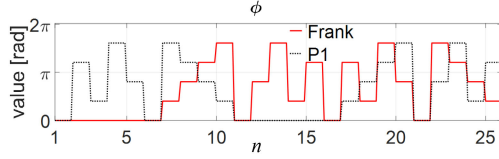| Modulation scheme	Parameters	Range
LFM	f_c B N	$7f_s/40$ $f_s/10$ 800
Costas	Costas sequence $f_{\min}$ N	$\{4, 2, 5, 1, 3\}$ $3f_s/80$ 800
BPSK	L_c f_c N_{cc}	13 $7f_s/40$ 14
Frank , P1	f_c N_{cc} M	$7f_s/40$ 5 6
P2	f_c N_{cc} M	$7f_s/40$ 6 6
P3$_o$	f_c N_{cc} ρ	$7f_s/40$ 6 25
P3$_e$, P4	f_c N_{cc} ρ	$7f_s/40$ 6 36
T1, T2	f_c N_g N	$7f_s/40$ 5 800
T3, T4	f_c ΔF N	$7f_s/40$ $f_s/20$ 800

Fig. 15. Phase offset values of Frank and P1 signals for $M = 5$.

APPENDIX B
PROOF OF ANALOGIES FOR CW POLYPHASE SIGNALS

1) Analogy between Frank and P1 signals for odd M
The phase offset values of Frank and P1 signals for one pulse interval are defined as follows [1],

$$\phi_{Fr}[i_{Fr}, j_{Fr}] = \frac{2\pi}{M}(i_{Fr} - 1)(j_{Fr} - 1), \qquad (10)$$

$$\phi_{P1}[i_{P1}, j_{P1}] = \frac{2\pi}{M}\left[i_{P1} - 1 + M(j_{P1} - 1)\right]$$

$$\times \left(j_{P1} - \frac{M+1}{2}\right), \qquad (11)$$

where $i_{Fr}, i_{P1} = 1, 2, \ldots M$, and $j_{Fr}, j_{P1} = 1, 2, \ldots M$. The one-dimensional phase offset values $\phi_{Fr}[n_{Fr}]$ and $\phi_{P1}[n_{P1}]$ are formed by concatenating the rows of $\phi_{Fr}[i_{Fr}, j_{Fr}]$ and $\phi_{P1}[i_{P1}, j_{P1}]$, respectively [27]. Therefore, the phase offset index n_{Fr} can be calculated from i_{Fr}, j_{Fr}, and M by the formula:

$$n_{Fr} = M \times j_{Fr} + i_{Fr}. \qquad (12)$$

A similar formula can also be derived for n_{P1}.

Fig. 15 shows $\phi_{Fr}[n_{Fr}]$ and $\phi_{P1}[n_{P1}]$ for $M = 5$. As can be seen, $\phi_{P1}[n_{P1}]$ is identical to $\phi_{Fr}[n_{Fr}]$ shifted circularly by 10 units in n_{Fr}. By observing that $\frac{M \times (M-1)}{2} = 10$ for $M = 5$, we predict that $\phi_{P1}[n_{P1}]$ is identical to $\phi_{Fr}[n_{Fr}]$ shifted circularly by $\frac{M \times (M-1)}{2}$ in n_{Fr}. We confirm this claim using the mathematical derivation, as in the following.

From equation (12), a circular shift by $\frac{M \times (M-1)}{2}$ in n_{Fr} corresponds to a circular shift by $\frac{M-1}{2}$ in j_{Fr} and no shift in i_{Fr}.

Let $j_{P1} = j_{Fr} + \frac{M-1}{2}$, and $i_{P1} = i_{Fr}$,

$$\phi_{P1}[i_{P1}, j_{P1}] = \frac{2\pi}{M}\left[i_{Fr} - 1 + M\left(j_{Fr} + \frac{M-1}{2} - 1\right)\right]$$

$$\times \left(j_{Fr} + \frac{M-1}{2} - \frac{M+1}{2}\right)$$

$$= \frac{2\pi}{M}(i_{Fr} - 1)(j_{Fr} - 1)$$

$$+ 2\pi\left(j_{Fr} + \frac{M-3}{2}\right)(j_{Fr} - 1)$$

$$= \phi_{Fr}[i_{Fr}, j_{Fr}] + 2\pi\left(j_{Fr} + \frac{M-3}{2}\right)(j_{Fr} - 1). \qquad (13)$$

For the second term on the right side of equation (13), we have $2\pi(j_{Fr} + \frac{M-3}{2})(j_{Fr} - 1)$, which is a multiple of 2π because $(j_{Fr} + \frac{M-3}{2})(j_{Fr} - 1)$ is an integer when M is odd. Due to the periodicity of any angle with a period of 2π, we can eliminate $2\pi(j_{Fr} + \frac{M-3}{2})(j_{Fr} - 1)$ without changing the actual value of $\phi_{P1}[i_{P1}, j_{P1}]$.

Therefore, $\phi_{P1}[i_{P1}, j_{P1}] = \phi_{Fr}[i_{Fr}, j_{Fr}]$ when $j_{P1} = j_{Fr} + \frac{M-1}{2}$ and and $i_{P1} = i_{Fr}$. As a result, for odd M, Frank and P1 signals are just time-delayed versions of each other and are considered in this paper as Frank$_o \vee$P1$_o$.

2) Analogy between P3 and P4 signals for even M
The phase offset formulas of P3 and P4 signals are defined as the following [1],

$$\phi_{P3}[i_{P3}] = \frac{\pi}{M^2}(i_{P3} - 1)^2 = \frac{\pi}{\rho}(i_{P3} - 1)^2, \qquad (14)$$

$$\phi_{P4}[i_{P4}] = \frac{\pi}{M^2}(i_{P4} - 1)^2 - \pi(i_{P4} - 1)$$

$$= \frac{\pi}{\rho}(i_{P4} - 1)^2 - \pi(i_{P4} - 1), \qquad (15)$$

where $i_{P3}, i_{P4} = 1, 2, \ldots \rho$.

Similar to the case of Frank and P1 signals, when M is even, $\phi_{P3}[i_{P3}]$ is identical to $\phi_{P4}[i_{P4}]$ shifted circularly by $\frac{\rho}{2}$ units in i_{P4}, or is identical to $\phi_{P4}[i_{P4}] + \pi$ shifted circularly by $\frac{\rho}{2}$ units in i_{P4}. We confirm this claim using the mathematical derivation, as in the following.
Let $i_{P3} = i_{P4} + \frac{\rho}{2}$,

$$\phi_{P3}[i_{P3}] = \frac{\pi}{\rho}\left(i_{P4} - 1 + \frac{\rho}{2}\right)^2$$

$$= \frac{\pi}{\rho}(i_{P4} - 1)^2 - \pi(i_{P4} - 1) + \frac{\pi\rho}{4}$$

$$= \phi_{P4}[i_{P4}] + \frac{\pi\rho}{4}. \qquad (16)$$

- M is divisible by 4
Let $M = 4K$, where K is an arbitrary integer. Substituting the value of M into the second term on the right side of equation (16), we have

$$\frac{\pi\rho}{4} = \frac{\pi M^2}{4} = 4\pi K^2. \qquad (17)$$

The term $4\pi K^2$ of equation (17) is a multiple of 2π. As a result, the term $\frac{\pi\rho}{4}$ on the right side of equation (16) can be eliminated without changing the actual value of $\phi_{P3}[i_{P3}]$.
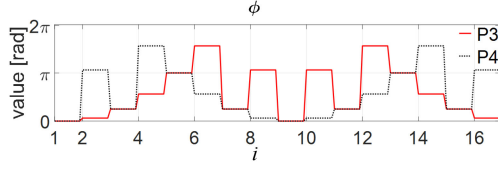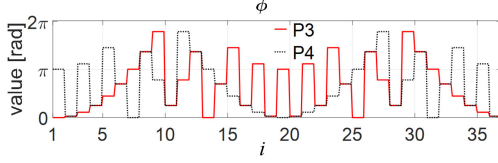Therefore, $\phi_{P3}[i_{P3}] = \phi_{P4}[i_{P4}]$ when M is odd and divisible by 4, and $i_{P3} = i_{P4} + \frac{\rho}{2}$.
Fig. 16 shows $\phi_{P3}[i_{P3}]$ and $\phi_{P4}[i_{P4}]$ for $M = 4$. As can be seen, $\phi_{P3}[i_{P3}]$ is identical to $\phi_{P4}[i_{P4}]$ shifted circularly by $\frac{\rho}{2}$ (e.g., = 8 for $M = 4$) units in i_{P4}.

- M is not divisible by 4
Let $M = 4K + 2$, where K is an arbitrary integer. Substituting the value of M into the second term on the right side of equation (16), we have

$$\frac{\pi\rho}{4} = \frac{\pi M^2}{4} = 4\pi K^2 + 4\pi K + \pi. \qquad (18)$$

Fig. 16. Phase offset value of P3 and P4 signals for $M = 4$.

Fig. 17. Phase offset value of P3 signal and $\pi+$ phase offset value of P4 signals for $M = 6$.

(a)

(b)

Fig. 18. (a) Difference between consecutive phase offset values for $M = 5$, (b) CWD-TFI of P3 signals for $M = 5$.

The term $4\pi K^2 + 4\pi K$ on the right side of equation (18) can be eliminated because it is a multiple of 2π. Therefore, when M is odd and not divisible by 4, and $i_{P3} = i_{P4} + \frac{\rho}{2}$, we have

$$\phi_{P3}[i_{P3}] = \phi_{P4}[i_{P4}] + \pi. \qquad (19)$$

Fig. 17 shows the values of $\phi_{P3}[i_{P3}]$ and $\phi_{P4}[i_{P4}] + \pi$ for $M = 6$. As shown, $\phi_{P3}[i_{P3}]$ is identical to $\phi_{P4}[i_{P4}] + \pi$ shifted circularly by $\frac{\rho}{2}$ (e.g., $= 18$ for $M = 6$) units in i_{P4}.

Note that an additional constant phase shift of π in equation (19) merely causes an additional time delay for the P3 signal. Therefore, as long as M is even, P3 and P4 signals are just time-delayed versions of each other and are considered in this paper as $\text{P3}_e \vee \text{P4}_e$.

APPENDIX C

PROOF OF POWER SPECTRUM SEPARATION BETWEEN TWO CONSECUTIVE PULSE INTERVALS OF P3 SIGNAL WHEN M IS ODD

Let $\triangle_\phi$ be the difference between consecutive phase offset values of the polyphase signals, that is:

$$\triangle_\phi[i] = \phi[i+1] - \phi[i]. \qquad (20)$$

Fig. 18 shows $\triangle_{\phi_{P3}}[i_{\triangle_{P3}}]$ that is the $\triangle_\phi$ of P3 signals, and its corresponding CWD-TFI for $M = 5$ over two complete pulse intervals. As can be seen, there are three regions in which $\triangle_{\phi_{P3}}[i_{\triangle_{P3}}]$ is close to π, as illustrated by the red circles in Fig. 18(a), corresponds to the three power spectrum separations in the signal objects in CWD-TFI, as illustrated by the white circles in Fig. 18(b). Among the three power spectrum separations, the second power spectrum separation (i.e., at $i_{\triangle_{P3}} = 25$) is due to the transition between two consecutive pulse intervals, whereas the first and the third power spectrum separations (i.e., at $i_{\triangle_{P3}} = 14$ and $i_{\triangle_{P3}} = 39$, respectively) are due to the large phase increment in the middle of P3 pulse interval [1], [5]. Note also on CWD-TFI in Fig. 18(b) that the second power spectrum separation is much narrower than the first and the third ones. This is because the second power spectrum separation is due to only a sudden $\triangle_{\phi_{P3}}[i_{\triangle_{P3}}]$ value close to π, whereas the other
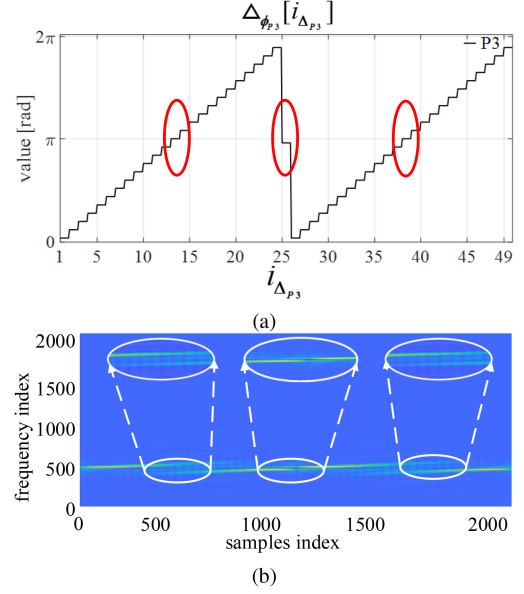
(a)

(b)
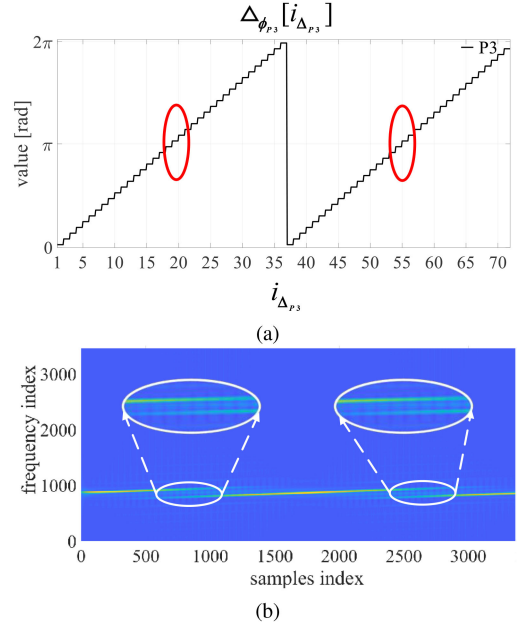
Fig. 19. (a) Difference between consecutive phase offset values for $M = 6$, (b) CWD-TFI of P3 signals for $M = 6$.

power spectrum separations are due to consecutive $\triangle_{\phi_{P3}}[i_{\triangle_{P3}}]$ values close to π.

Fig. 19 shows $\triangle_{\phi_{P3}}[i_{\triangle_{P3}}]$ and its corresponding CWD-TFI for $M = 6$ over two complete pulse intervals. As can be seen, there are only two regions in which $\triangle_{\phi_{P3}}[i_{\triangle_{P3}}]$ is close to π, as illustrated by the red circles in Fig. 19(a); these regions correspond to two power spectrum separations in the CWD-TFIs, as illustrated by the white circles in Fig. 19(b). All of this is because the value of $\triangle_{\phi_{P3}}[i_{\triangle_{P3}}]$ at the transition between two consecutive pulse intervals (i.e., at $i_{\triangle_{P3}} = 36$) is not close to π,

as shown in Fig. 19(a), resulting in no power spectrum separation at this position. In summary, depending on M (i.e., odd or even), the CW P3 signal results in two different signal objects in CWD-TFI, such as $P3_o$ and $P3_e$.

The values of $\triangle_\phi$ in the transitions between two consecutive pulse intervals of the Frank, P1, P2, and P4 signals, similar to that of the $P3_e$ signal, are close to 0. Therefore, there is no power spectrum separation between two consecutive pulse intervals of the Frank, P1, P2, and P4 signals. Therefore, only the CW P3 signal results in two different signal objects in CWD-TFI.

REFERENCES

[1] P. E. Pace, *Detecting and Classifying Low Probability of Intercept Radar*. Norwood, MA, USA: Artech House, 2009.

[2] M. A. Richards, J. Scheer, W. A. Holm, and W. L. Melvin, *Principles of Modern Radar*. Chennai, India: SciTech Publishing, 2010.

[3] J. Lundén and V. Koivunen, "Automatic radar waveform recognition," *IEEE J. Sel. Topics Signal Process.*, vol. 1, no. 1, pp. 124–136, Jun. 2007.

[4] M. Zhang, L. Liu, and M. Diao, "LPI radar waveform recognition based on time-frequency distribution," *Sensors*, vol. 16, no. 10, 2016, Art. no. E1682.

[5] S.-H. Kong, M. Kim, L. M. Hoang, and E. Kim, "Automatic LPI radar waveform recognition using CNN," *IEEE Access*, vol. 6, pp. 4207–4219, 2018.

[6] M. Zhang, M. Diao, and L. Guo, "Convolutional neural networks for automatic cognitive radio waveform recognition," *IEEE Access*, vol. 5, pp. 11074–11082, 2017.

[7] T. R. Kishore and K. D. Rao, "Automatic intrapulse modulation classification of advanced LPI radar waveforms," *IEEE Trans. Aerosp. Electron. Syst.*, vol. 53, no. 2, pp. 901–914, Apr. 2017.

[8] D. Yeom and P. E. Pace, "Extending CW radar unambiguous detection range using a modified frank code," in *Proc. IEEE Radar Conf.*, 2018, pp. 1365–1370.

[9] T. O. Gulum, A. Y. Erdogan, T. Yildirim, and L. D. Ata, "Parameter extraction of FMCW modulated radar signals using Wigner-Hough transform," in *Proc. IEEE 12th Int. Symp. Comput. Intell. Informat.*, 2011, pp. 465–468.

[10] A. Y. Erdogan, T. O. Gulum, L. Durak-Ata, T. Yildirim, and P. E. Pace, "FMCW signal detection and parameter extraction by cross Wigner–Hough transform," *IEEE Trans. Aerosp. Electron. Syst.*, vol. 53, no. 1, pp. 334–344, Feb. 2017.

[11] B. M. Hamschin, J. D. Ferguson, and M. T. Grabbe, "Interception of multiple low-power linear frequency modulated continuous wave signals," *IEEE Trans. Aerosp. Electron. Syst.*, vol. 53, no. 2, pp. 789–804, Apr. 2017.

[12] Z. Qiu, J. Zhu, and F. Li, "Multiple BPSK/LFM Hybrid modulated signals parameter estimation and analysis intercepted by non-cooperative radar receiver," in *Proc. IEEE Int. Conf. Comput. Electromagn.*, 2018, pp. 1–4.

[13] W. Liu *et al.*, "SSD: Single shot multibox detector," in *Proc. Eur. Conf. Comput. Vision*, 2016, pp. 21–37.

[14] S. J. Russell and P. Norvig, *Artificial Intelligence: A Modern Approach*. Kuala Lumpur, Malaysia: Pearson Education Limited, 2016.

[15] B. Boashash, *Time-Frequency Signal Analysis and Processing: A Comprehensive Reference*. New York, NY, USA: Academic, 2015.

[16] Z. M. Hussain and B. Boashash, "Adaptive instantaneous frequency estimation of multicomponent FM signals using quadratic time-frequency distributions," *IEEE Trans. Signal Process.*, vol. 50, no. 8, pp. 1866–1876, Aug. 2002.

[17] L. Stankovic and S. Stankovic, "On the Wigner distribution of discrete-time noisy signals with application to the study of quantization effects," *IEEE Trans. Signal Process.*, vol. 42, no. 7, pp. 1863–1867, Jul. 1994.

[18] L. Cohen, "Time-frequency distributions—A review," *Proc. IEEE*, vol. 77, no. 7, pp. 941–981, Jul. 1989.

[19] H.-I. Choi and W. J. Williams, "Improved time-frequency representation of multicomponent signals using exponential kernels," *IEEE Trans. Acoust., Speech, Signal Process.*, vol. 37, no. 6, pp. 862–871, Jun. 1989.

[20] A. Naït-Ali, *Advanced Biosignal Processing*. Berlin, Germany: Springer Science & Business Media, 2009.

[21] J. A. Parker, R. V. Kenyon, and D. E. Troxel, "Comparison of interpolating methods for image resampling," *IEEE Trans. Med. Imag.*, vol. MI-2, no. 1, pp. 31–39, Mar. 1983.

[22] T.-Y. Lin *et al.*, "Microsoft COCO: Common objects in context," in *Proc. Eur. Conf. Comput. Vision*, 2014, pp. 740–755.

[23] A. G. Howard, "Some improvements on deep convolutional neural network based image classification," 2013, arXiv:1312.5402.

[24] T. O. Gulum, P. E. Pace, and R. Cristi, "Extraction of polyphase radar modulation parameters using a Wigner-Ville distribution-Radon transform," in *Proc. IEEE Int. Conf. Acoust., Speech, Signal Process.*, 2008, pp. 1505–1508.

[25] E. Chassande-Mottin and A. Pai, "Discrete time and frequency Wigner-Ville distribution: Moyal's formula and aliasing," *IEEE Signal Process. Lett.*, vol. 12, no. 7, pp. 508–511, Jul. 2005.

[26] R. Girshick, J. Donahue, T. Darrell, and J. Malik, "Rich feature hierarchies for accurate object detection and semantic segmentation," in *Proc. IEEE Conf. Comput. Vision Pattern Recognit.*, 2014, pp. 580–587.

[27] N. Levanon and E. Mozeson, *Radar Signals*. Hoboken, NJ, USA: Wiley, 2004.
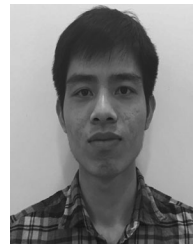
Linh Manh Hoang received the B.S. degree in mechatronics engineering from Hanoi University of Science and Technology, Hanoi, Vietnam, in 2012, and the M.S. degree in electrical engineering from the Korea Advanced Institute of Science and Technology, Daejeon, South Korea, in 2019. He is currently working toward the Ph.D. degree with the Faculty of Engineering and Information Technology, University of Technology Sydney, Ultimo, NSW, Australia. His research interests include signal processing, radar, deep learning, and wireless communication.

Minjun Kim received the B.S. degree in electrical and electronics engineering from Chung-Ang University, Seoul, South Korea, in 2017, and the M.S. degree from the CCS Graduate School of Green Transportation, Korea Advanced Institute of Science and Technology, Daejeon, South Korea, in 2019. Since 2019, he has been with Korea Aerospace Research Institute, Daejeon, South Korea. His research interests include signal processing, RADAR, LiDAR, machine learning, deep learning, and satellite system.
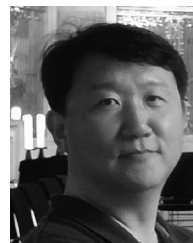
Seung-Hyun Kong (M'06–SM'16) received B.S. degree in electronics engineering from Sogang University, Seoul, South Korea, in 1992, the M.S. degree in electrical engineering from Polytechnic University, New York, NY, USA, in 1994, and the Ph.D. degree in aeronautics and astronautics from Stanford University, Stanford, CA, USA, in January 2006. From 1997 to 2004, he was with Samsung Electronics, Inc., and Nexpilot, Inc., both in South Korea, where he worked on developing wireless communication system standards and UMTS mobile positioning technologies. In 2006 and from 2007 to 2009, he was a Staff Engineer with Polaris Wireless, Inc., Santa Clara, and at Qualcomm, Inc. (Corp. R&D), San Diego, respectively, where his research was on assisted-GNSS and wireless positioning technologies. Since 2010, he has been with Korea Advanced Institute of Science and Technology, Daejeon, South Korea, where he is currently an Associate Professor with the CCS Graduate School of Green Transportation. His research interests include signal processing for GNSS and vehicle sensors, and deep neural networks for vehicular sensing and autonomous driving systems. He is an Editor for *IET Radar, Sonar and Navigation*, and an Associate Editor for the IEEE TRANSACTIONS ON INTELLIGENT TRANSPORTATION SYSTEMS and IEEE ACCESS. He is also the Lead Guest Editor for the Special Section on "GNSS, Positioning, and Navigation Technologies" in IEEE ACCESS and the Special Issue on "Intelligent Transportation Systems empowered by AI technologies" in the IEEE TRANSACTIONS ON INTELLIGENT TRANSPORTATION SYSTEMS.